Journal of
Synchrotron
Radiation

ISSN 1600-5775

Received 27 June 2014
Accepted 1 September 2014

A portable ultrahigh-vacuum system for advanced synchrotron radiation studies of thin films and nanostructures: $EuSi_2$ nano-islands

Shyjumon Ibrahimkutty,[a,b]‡ Anja Seiler,[a,b] Tim Prüßmann,[c] Tonya Vitova,[c] Ramu Pradip,[a,b] Olga Bauder,[a,b] Peter Wochner,[d] Anton Plech,[b] Tilo Baumbach[a,b,e] and Svetoslav Stankov[a,b]*

[a]Laboratory for Applications of Synchrotron Radiation, Karlsruhe Institute of Technology, D-76131 Karlsruhe, Germany, [b]Institute for Photon Science and Synchrotron Radiation, Karlsruhe Institute of Technology, D-76344 Eggenstein-Leopoldshafen, Germany, [c]Institute for Nuclear Waste Disposal, Karlsruhe Institute of Technology, D-76344 Eggenstein-Leopoldshafen, Germany, [d]Max Planck Institute for Solid State Research, 70569 Stuttgart, Germany, and [e]Synchrotron Radiation Facility ANKA, Karlsruhe Institute of Technology, D-76344 Eggenstein-Leopoldshafen, Germany.
*E-mail: svetoslav.stankov@kit.edu

A portable ultrahigh-vacuum system optimized for *in situ* variable-temperature X-ray scattering and spectroscopy experiments at synchrotron radiation beamlines was constructed and brought into operation at the synchrotron radiation facility ANKA of the Karlsruhe Institute of Technology, Germany. Here the main features of the new instrument are described and its capabilities demonstrated. The surface morphology, structure and stoichiometry of $EuSi_2$ nano-islands are determined by *in situ* grazing-incidence small-angle X-ray scattering and X-ray absorption spectroscopy. A size reduction of about a factor of two of the nano-islands due to silicide decomposition and Eu desorption is observed after sample annealing at 1270 K for 30 min.

Keywords: *in situ* experiments; GISAXS; EXAFS; XANES; rare-earth silicides.

1. Introduction

Nanoscale materials supported on a substrate exhibiting various surface morphologies, such as nano-clusters, -islands and -wires, have the potential to contribute immensely to various areas spanning energy, information technology and environmental research. The comprehensive morphology and structure characterization of such nanoscale objects is of fundamental importance for understanding the relationship of structure, shape and size to the physical properties and for their optimization and tailoring for specific applications.

The rapid development of synchrotron radiation sources combined with the progress of the X-ray optics and detectors during the last decades has offered the scientific community X-ray beams with enormously high brilliance focused on spots with micro- and nanometer dimensions. That facilitated the establishment of advanced X-ray scattering and spectroscopy methods as standard tools for non-destructive characterization of materials with dimensions on the nanometer length scale and of processes down to the nanosecond time scale. These investigations, however, require the development of dedicated instrumentation and sample environment in order to prepare the nanostructures and to investigate their crystallographic structure, morphology and the desired properties under controlled, very often ultrahigh-vacuum (UHV), conditions. In response to these needs for instrumentation, various vacuum and ultrahigh-vacuum multifunctional chambers optimized for *in situ* experiments with synchrotron radiation have been constructed and brought into operation (*e.g.* Döhrmann *et al.*, 2013; Krause *et al.*, 2012; Slobodskyy *et al.*, 2012; Couet *et al.*, 2008; Stankov *et al.*, 2008).

The increasingly important applications of rare-earth (RE)-based nanostructures in various fields such as micro- and nanoelectronics, catalysts, hydrogen storage and magnetism have motivated their intensive research in recent years. Among them the ultrathin RE sesquioxide films (high-*k* materials) and the self-organized RE silicide (RESi) nanostructures attract particular attention because of their relevance to the CMOS nanoelectronics. While the RESi nanowires have the potential to serve as ohmic contacts and interconnects in future nanoelectronics (Snider & Williams, 2007), the high-*k* layers have already replaced the SiO_2 gate layer in the nano-MOSFETs (Fanciulli & Scarel, 2007). For such applications, however, the investigation of the thermal stability of the crystal phases and their morphology is essential since the heat dissipation became a demanding issue with the

‡ Present address: Max Planck Institute for Solid State Research, 70569 Stuttgart, Germany.

continuous downscaling of the electronic devices (Balandin, 2011).

To address these challenges we have designed and brought into operation a new portable UHV analysis chamber dedicated to variable-temperature *in situ* (under ultrahigh-vacuum conditions) X-ray scattering and spectroscopy experiments at synchrotron radiation sources. In this paper we describe the main features of the instrument and demonstrate its capabilities by *in situ* study of the surface morphology, stoichiometry and crystal structure of europium silicide nano-islands applying grazing-incidence small-angle X-ray scattering (GISAXS) and X-ray absorption spectroscopy (XAS).

2. Experimental details

2.1. A portable UHV analysis chamber for *in situ* scattering and spectroscopy experiments with synchrotron radiation

The UHV analysis chamber, delivered by CreaTec Fischer & Co. GmbH (http://www.createc.de), is stationed at the UHV-Analysis laboratory of the synchrotron radiation source ANKA in close vicinity to the scattering and spectroscopy beamlines. The chamber can be docked to the existing UHV-cluster in order to transfer the samples grown by molecular beam epitaxy and characterized by the available analytical methods such as reflection high-energy electron diffraction (RHEED), low-energy electron diffraction (LEED), Auger electron spectroscopy (AES), X-ray photo-electron spectroscopy (XPS) and scanning probe microscopy (AFM/STM).

The body of the chamber is based on a 200 CF flange and can be docked to the UHV cluster at ANKA as well as to other UHV systems through a 40 CF port. The distance from the sample surface to the surface of the heavy-duty diffractometer is set by design to 170 mm (or higher) allowing for mounting the UHV chamber on the two-circle segment cradle Huber 5203.20 (or 5203.80).

The heart of the UHV analysis chamber is the sample manipulator that allows for a motorized (Faulhaber DC servo motor) unlimited sample rotation around the surface normal. By decoupling from the motor, the sample can also be rotated manually. The sample rotation is particularly useful for GISAXS and surface diffraction experiments. A pneumatically actuated stamp fixes the sample holder to the manipulator by pressing it against the manipulator head, thus fixing the azimuthal angle during the experiments.

The sample manipulator is equipped with an integrated heater unit for resistive sample heating up to 1300 K. A thermocouple attached near the tungsten filament is used for temperature control and regulation. An integrated liquid-nitrogen tank ensures cooling the sample holders down to about 140 K. This tank can be coupled to the manipulator head with a clamping bracket that serves as a thermal bridge. A second thermocouple attached to the tank is used for temperature control during sample cooling.

Substrates with dimensions up to one inch can be mounted on the molybdenum sample holder. A sample storage compartment with the capacity to store up to five sample holders is an integral part of the UHV chamber. It is mounted on 16 CF feedthrough, allowing for 360° rotation around its axis and for vertical adjustment during the samples transfer. In order to protect the stored samples while heating the investigated sample, the storage compartment can be rotated by 180° exposing only the thermally shielded backside to the radiated heat from the manipulator. A wobble stick is used to transfer the samples between the storage compartment and the sample manipulator.

Depending on the desired experiments the UHV analysis chamber can be used in three different configurations described in detail below.

2.1.1. Configuration A. Configuration A, Fig. 1(*a*), is optimized for XAS, high energy resolution X-ray absorption near-edge structure (HR-XANES), resonant X-ray emission (RXES) and resonant inelastic X-ray scattering (RIXS) studies on thick films and nanostructures. These investigations

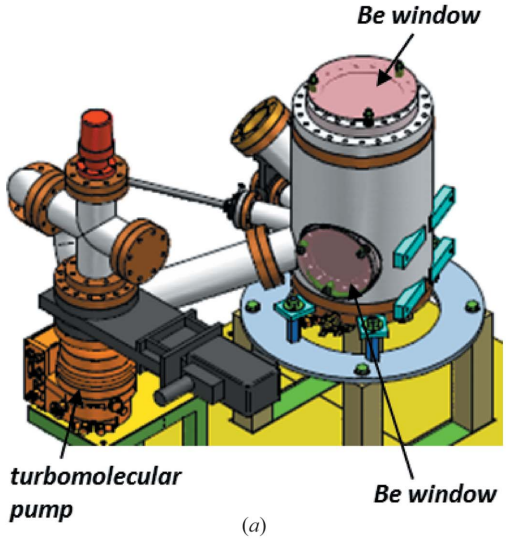

Figure 1
(*a*) Schematic view of the portable UHV analysis chamber in configuration A. (*b*) Photograph of the experimental setup for *in situ* XAS experiments at the INE beamline of ANKA. In this configuration the TMP is directly mounted on the chamber.

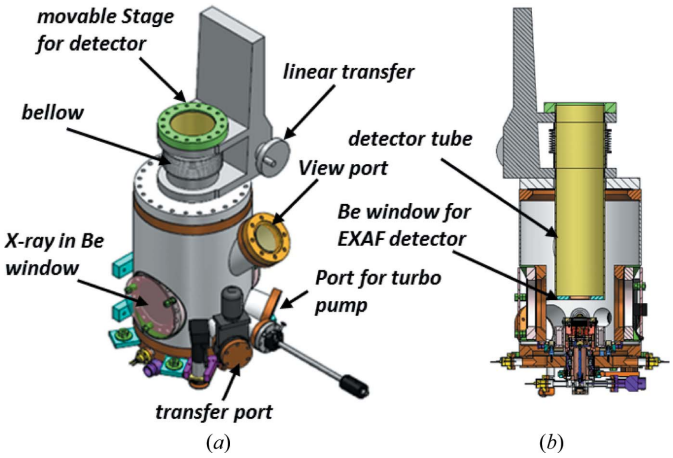

Figure 2
(*a*, *b*) Schematic views of the portable UHV analysis chamber in configuration B. The turbomolecular pump is omitted for simplicity.

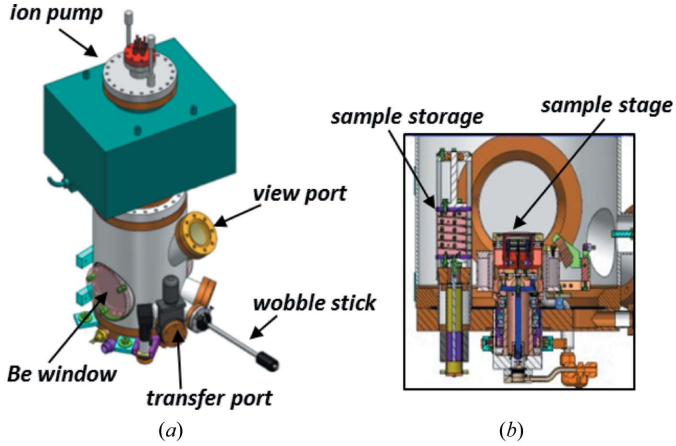

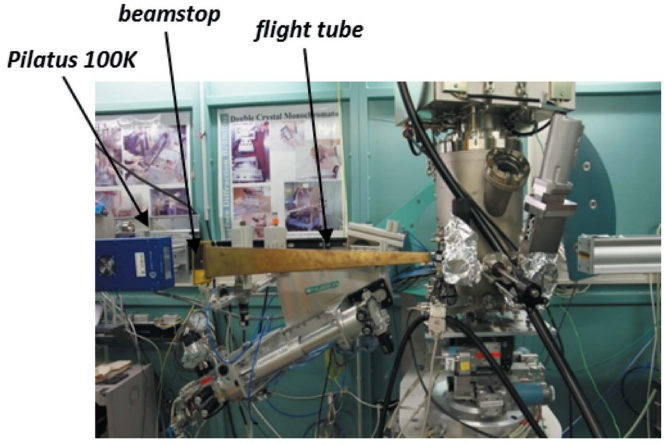

Figure 3
Schematic view of (*a*) the portable UHV analysis chamber in configuration C and (*b*) the sample manipulator and the sample storage compartment. (*c*) Photograph of the experimental setup for *in situ* GISAX experiments at the MPI diffraction beamline of ANKA.

are facilitated by a 0.5 mm-thick Be window diffusion bonded on a 160 CF flange providing a large solid angle that is a prerequisite for these experiments. A base pressure of about 8×10^{-10} mbar is ensured by a Pfeiffer Hi space 300 turbomolecular pump (TMP) directly connected to the UHV chamber *via* a 63 CF flange (Fig. 1*b*). In this configuration the chamber is mounted sidewise providing a vertical sample orientation that is favorable for the X-ray spectroscopy experiments. For the XAS experiments an energy-dispersive solid-state detector is placed at 90° to the incident beam in the horizontal plane, in order to minimize the background from the Thomson-scattered X-rays (Fig. 1*b*).

2.1.2. Configuration B. Temperature-dependent XAS experiments on thin and ultrathin films and nanostructures of sub-monolayer coverages are possible by using configuration B of the UHV chamber, Figs. 2(*a*) and 2(*b*). In this configuration the large Be window from configuration A is replaced by a movable detector stage mounted on a 100 CF linear transfer with a stroke of 150 mm. The detector stage ends with a 63 CF Be window that can approach the sample surface as close as about 5 mm, thus covering a large solid angle. Positioning the detector stage at the top-most position automatically closes a shutter that protects the Be window from contamination by possible evaporation of material during the high-temperature annealing of the samples. Similarly to configuration A (Fig. 1*b*), the UHV condition is ensured by the turbomolecular pump directly connected to the chamber.

2.1.3. Configuration C. Configuration C is designed for vertical mounting of the chamber on a heavy-duty diffractometer. This configuration is dedicated to *in situ* grazing-incidence X-ray diffraction and GISAXS experiments. Fig. 3(*a*) shows a schematic view of the chamber in this configuration. Details of the manipulator and the sample storage compartment are shown in Fig. 3(*b*). A 300 l s^{-1} ion pump (Gamma Vacuum) mounted on the top of the chamber ensures a base pressure of 2×10^{-10} mbar. A titanium sublimation pump and a cryo-shroud can be used to further reduce the pressure to about 4×10^{-11} mbar. Two diametrical 100 CF flanges with 0.5 mm-thick diffusion-bounded Be foils serve as X-ray entrance and exit windows ensuring a free aperture of 108 mm (∼35°). A photograph of the UHV analysis chamber in this configuration mounted on the heavy-duty diffractometer at the MPI beamline of ANKA is shown in Fig. 3(*c*). The vacuum flight tube, beamstop and Pilatus 100K detector are also visible.

2.2. Sample growth

Europium silicide with Eu coverages of 1.0 nm (islands) and 100 nm (film) were grown by molecular beam epitaxy in the growth chamber of the UHV-Analysis laboratory at ANKA, Karlsruhe Institute of Technology (KIT), Germany. The vacuum-outgassed metallic Eu, supplied by the Ames laboratory, was sublimated from an effusion cell equipped with a PBN crucible on an n-type (P-doped, 10 Ω cm) 20 mm × 20 mm × 1.0 mm Si(001) vicinal substrate with a miscut of 4° towards [110]. Details of the growth procedure can be found elsewhere (Seiler *et al.*, 2014).

Commercially available Eu_2O_3 in powder form mixed with 100 mg of BN and pressed into a pellet of diameter 13 mm was used as a reference in the XAS experiments.

2.3. *In situ* XAS at the INE beamline of ANKA

The high-brilliance synchrotron radiation sources and advanced X-ray optics and detectors increased the detection limit of the X-ray absorption/emission spectroscopy experiments and allowed for rapid development of photon-demanding methods such as RIXS and HR-XANES (de Groot & Kotani, 2008; Glatzel *et al.*, 2009; Vitova *et al.*, 2010). While XANES is an effective method for determination of the average oxidation state (Vitova *et al.*, 2008), both XANES and the extended X-ray absorption near-edge structure (EXAFS) provide valuable information about the crystal structure.

Room-temperature Eu L_2-edge (7617 eV) EXAFS and L_3-edge (6977 eV) XANES spectra of europium silicide film and nano-islands as well as of a reference Eu_2O_3 sample were recorded at the INE beamline for actinide research (Rothe *et al.*, 2012) at ANKA. A double-crystal monochromator (DCM) equipped with a set of Si(111) crystals was employed for energy monochromatization of the incident X-ray beam. The EXAFS/XANES data of the europium silicide and the reference Eu_2O_3 sample were collected in fluorescence and transmission mode, respectively. A five-element Ge solid-state detector (Canberra LEGe type) was used for all measurements in fluorescence mode. At least six/two EXAFS/XANES spectra were collected in order to check the reproducibility of the spectral features and to improve the counting statistics. The DCM was calibrated by assigning 7112 eV to the first inflection point of a repeatedly measured Fe *K*-edge XANES spectrum of an α-Fe foil. The deposited nanostructures were illuminated with the X-ray beam at an incidence angle of approximately 30° using configuration A of the UHV analysis chamber (Fig. 1*b*).

2.4. *In situ* GISAXS experiments at the MPI beamline of ANKA

A wide variety of methods are presently available for the morphological characterization of nanoscale objects deposited on a substrate. Owing to its non-destructive nature, large investigated area (up to several millimeters) and high penetration depth of the X-rays, GISAXS was established as a unique method for investigating morphology and structure of surfaces and interfaces (Renaud, 1998; Levine *et al.*, 1989). The outstanding brilliance of the X-rays provided by the third-generation synchrotron radiation sources has reduced the data acquisition times down to the milliseconds range allowing for investigation of the nucleation processes and nanostructures growth in real time (Renaud *et al.*, 2003, 2004). Recent real-time studies on sputter-deposited films have shown that *in situ* synchrotron GISAXS combined with proper modeling can be used to understand the growth mechanism and various growth regimes of nanostructured films by extracting the morphology and the correlations of such nanostructures (Santoro *et al.*, 2014; Schwartzkopf *et al.*, 2013; Metwalli *et al.*, 2013; Yu *et al.*, 2013).

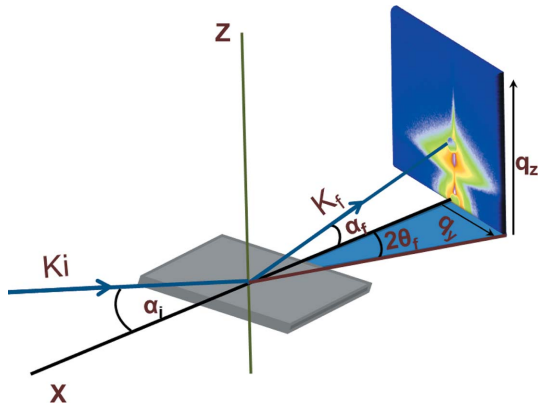

Figure 4
Grazing-incidence small-angle X-ray scattering geometry. $\mathbf{k}_i$ and $\mathbf{k}_f$ are, respectively, the incident and scattered wavevectors, α_i and α_f are the incident and the out-of-plane scattering angles, while $2\theta_f$ denotes the in-plane scattering angle. q_y and q_z are the momentum transfers along y and z, respectively.

In GISAXS geometry, the incident X-ray beam with a wavevector $\mathbf{k}_i$ impinges on the sample at a glancing angle α_i, close to the critical angle α_c, as illustrated in Fig. 4. The X-rays are scattered off from the sample surface with a wavevector $\mathbf{k}_f$, at an angle α_f with respect to the sample surface and at an in-plane angle $2\theta_f$ with respect to the transmitted beam. The resultant momentum transfer, $\mathbf{Q} = \mathbf{k}_i - \mathbf{k}_f$, can be decomposed to x, y and z components as follows (Renaud, 1998):

$$\begin{aligned} q_x &= (2\pi/\lambda)(\cos 2\theta_f \cos \alpha_f - \cos \alpha_i), \\ q_y &= (2\pi/\lambda)(\sin 2\theta_f \cos \alpha_f), \\ q_z &= (2\pi/\lambda)(\sin \alpha_f + \sin \alpha_i), \end{aligned} \tag{1}$$

where λ is the wavelength of the incident beam. The sizes of the nanostructures are obtained from analysis of the cuts made from the two-dimensional GISAXS patterns recorded in the $q_y q_z$ plane.

The *in situ* GISAXS experiment was performed at the hard X-ray scattering beamline MPI (Stierle *et al.*, 2004) of ANKA using photons with energy of 12 keV. The beam size of 100 µm (vertical) and 300 µm (horizontal) was achieved by sagittally bent mirrors and a slit system. The GISAXS images were recorded using a Pilatus 100K (Dectris) pixel detector (487 × 190 pixels, 172 µm per pixel) positioned at a distance of 1.1 m from the sample. A cylindrical beam stop was placed before the detector. A photodiode that could be moved in and out of the X-ray beam, between the Pilatus detector and the beam-stop, was used for the alignment of the sample and the beam stop. Fig. 3(*c*) shows a photograph of the experimental setup at the MPI beamline.

3. Results and discussion

3.1. *In situ* XAS experiments on $EuSi_2$ film and nano-islands

In order to determine the stoichiometry and structure of the europium silicides, an *in situ* XAS study at the Eu L_2 and L_3

Table 1
Summary of the EXAFS results.

From left to right are listed: single scattering path (Path), coordination numbers (N), half-path length of the photo-electron obtained from the crystal structure equal to interatomic distances for single scattering paths [$R_{\rm eff}$ (Å)], half-path length of the photo-electron obtained from the fit [$R_{\rm eff} - \Delta R$ (Å)], energy shift of the ionization potential [ΔE (eV)], mean squared atomic displacement/Debye–Waller factors [σ^2 (Å^2)].

Path	N	$R_{\rm eff}$ (Å)	$R_{\rm eff} - \Delta R$ (Å) ± 0.01	ΔE (eV) ± 0.7	σ^2 (Å^2)
Eu–Si1†	4	3.11	3.15 ± 0.01	0.7	0.013 ± 0.001
Eu–Si2	8	3.26	–	0.7	0.013 ± 0.001
Eu–Eu1	4	4.03	4.00 ± 0.03	0.7	0.013 ± 0.001
Eu–Eu2	4	4.30	4.40 ± 0.05	0.7	0.013 ± 0.001

† One Eu–Si single scattering path with coordination number $N = 12$ is used in the fit.

absorption edges was performed employing configuration A of the UHV analysis chamber. The *ATHENA* and *ARTEMIS* program packages, part of the *IFEFFIT* software (Ravel & Newville, 2005), were applied for data reduction of the XANES/EXAFS spectra and modeling the EXAFS spectra, respectively. The scattering paths used to fit the EXAFS spectra were generated by the *FEFF9.6* code based on the multiple scattering theory (Rehr & Albers, 2000). The Fermi energy was accurately calculated by using the self-consistent field (SCF) card implying self-consistent calculation of the atomic scattering potentials. Europium silicide of type $EuSi_2$ with tetragonal crystal structure ($I4_1/amdS$), unit-cell parameters $a = 4.304$ (3) Å, $b = 4.304$ (3) Å, $c = 13.65$ (1) Å, $\alpha = \beta = \gamma = 90^\circ$ was used to generate the atomic coordinates for the initial structural model (ICSD 1454). The EXAFS signal $\chi(k)$ covering the k range 2.4–8 Å^{-1} was Fourier transformed FT[$\chi(k)k^w$] to R space using a k weighting $w = 1$, 2 or 3 and a Hanning window with window sills $dk = 2$. The *ARTEMIS* option for simultaneous fits with all three k weightings (1, 2 and 3) was used. Fits were performed in R space over the R = 1.9–4.5 Å range. The fitting procedure resulted in a very good agreement between the experiment and the model, *i.e.* a fit quality of 0.01 reporting about 1% difference between the data and the fit.

The Eu L_2-edge EXAFS spectra of the investigated silicide film and the obtained best fits are plotted in Fig. 5. The results from the EXAFS analysis are summarized in Table 1. The amplitude reduction factor S_0^2 was varied during the fit, 0.8 ± 0.1, whereas the Si and Eu coordination numbers were fixed. This value of S_0^2 is in a reasonable agreement with the calculated *FEFF9.6* code value, $S_0^2 = 0.95$. The average interatomic Eu—Si (3.15 ± 0.01 Å), Eu—Eu1 (4.00 ± 0.03 Å) and Eu—Eu2 (4.40 ± 0.05 Å) distances obtained from the EXAFS analysis slightly deviate from the distances Eu—Si (3.18 Å), Eu—Eu1 (4.03 Å) and Eu—Eu2 (4.30 Å) reported by X-ray diffraction studies (Evers *et al.*, 1977). Such difference is possible as EXAFS is a local atomic structure probe technique and, for example, the Eu atoms close to the surface also contribute to the signal, whereas X-ray diffraction is sensitive only to the long-range atomic order of the material. The obtained results from the analysis of the EXAFS data confirm

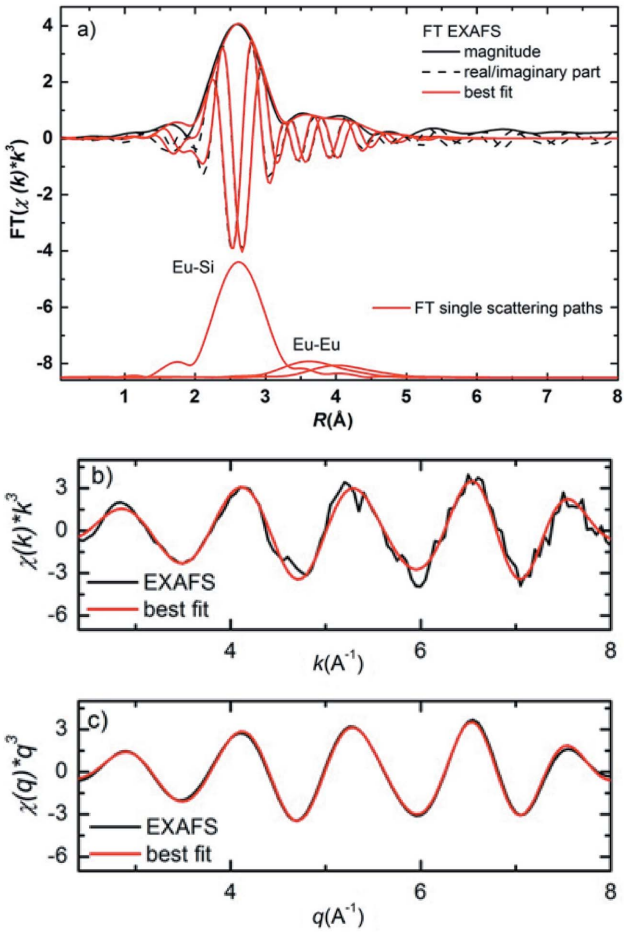

Figure 5
(*a*) Eu L_2-edge Fourier-transformed extended X-ray absorption fine structure (FT-EXAFS) spectrum of $EuSi_2$ film with Eu coverage of 100 nm (black) and best fits to data (red). The interatomic distance R (Å) is not phase-shift corrected in the figure. Vertically shifted are the contributions of the single scattering paths used in the modeling. EXAFS spectra and best fits (*b*) k^3-weighted and (*c*) q^3-weighted.

the assumed $EuSi_2$ stoichiometry and the tetragonal ($I4_1/amdS$) structure of the investigated europium silicide film.

An alternative to the EXAFS analysis is a qualitative analysis of the XANES part of the X-ray absorption fine-structure spectrum by comparison with the spectra of suitable reference compounds. XANES absorption resonances describe the multiple scattering of the photo-electron from the surrounding atoms. Therefore the spectrum fingerprints the short- and long-range atomic structure of the material.

Fig. 6 displays the Eu L_3-edge XANES spectra of the $EuSi_2$ nano-islands, the $EuSi_2$ film and the Eu_2O_3 reference. The energy position of the first inflection point of the spectra of the silicides is shifted with 5 eV to lower energy compared with the spectrum of Eu_2O_3. This energy shift is caused by more effective screening of the Eu $2p_{3/2}$ core-hole created in the X-ray absorption process and implies Eu oxidation state 2+ in $EuSi_2$ compared with 3+ in Eu_2O_3. The energy positions and shapes of the absorption resonances of the Eu L_3-edge XANES spectra of the $EuSi_2$ film and nano-islands are very similar, confirming that the nano-islands exhibit the $EuSi_2$

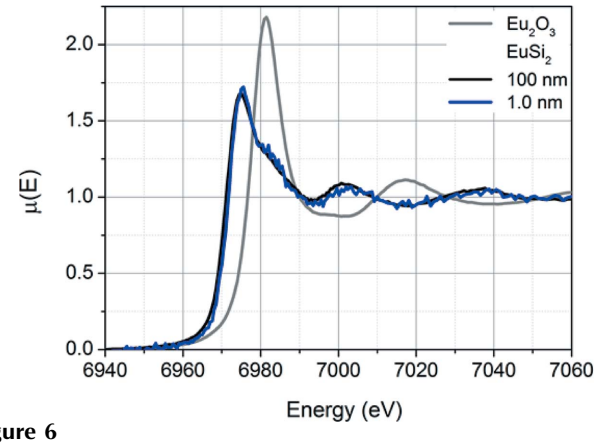

Figure 6
Eu L_3-edge XANES spectra of the Eu_2O_3 reference sample and the $EuSi_2$ film (100 nm) and nano-islands (1.0 nm).

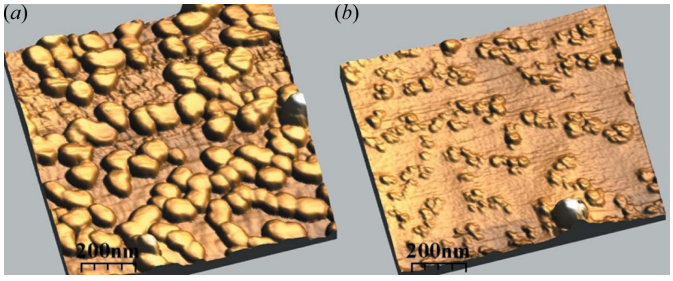

Figure 7
Contact-mode three-dimensional AFM images of the sample with Eu coverage of 1.0 nm obtained before (*a*) and after (*b*) the high-temperature annealing.

stoichiometry and the tetragonal ($I4_1/amdS$) structure found for the 100 nm-thick film by the EXAFS analysis. Owing to the low count rate, an EXAFS spectrum for Eu coverage of 1.0 nm in configuration A of the UHV analysis chamber was not feasible within the time frame of the experiment.[1]

3.2. *In situ* GISAXS studies of $EuSi_2$ nano-islands

In order to investigate the changes of the surface morphology upon high-temperature annealing of $EuSi_2$ nano-islands, GISAXS images were recorded at an incidence angle α_i of $\sim 0.3^\circ$, *i.e.* close to the critical angle of Si for 12 keV (0.14°) using configuration C of the UHV-Analysis chamber, Fig. 3(*c*). Fig. 7(*a*) shows an AFM image of the sample with Eu coverage of 1.0 nm, before the heat treatment, revealing the formation of conglomerates of three-dimensional islands with average dimensions 92 (5) nm × 98 (5) nm × 8(2) nm. The GISAXS images recorded with the wavevector being parallel and perpendicular to the steps of the vicinal Si(001) surface are depicted in Figs. 8(*a*) and 8(*b*), respectively. The acquisition time per frame was 20 s. The data are converted into one-dimensional scattering curves by making out-of-plane

[1] *In situ* variable-temperature EXAFS/XANES experiments on samples with sub-monolayer coverage of material will be possible in configuration B of the UHV analysis chamber that was still in the construction phase at the time of the experiment.

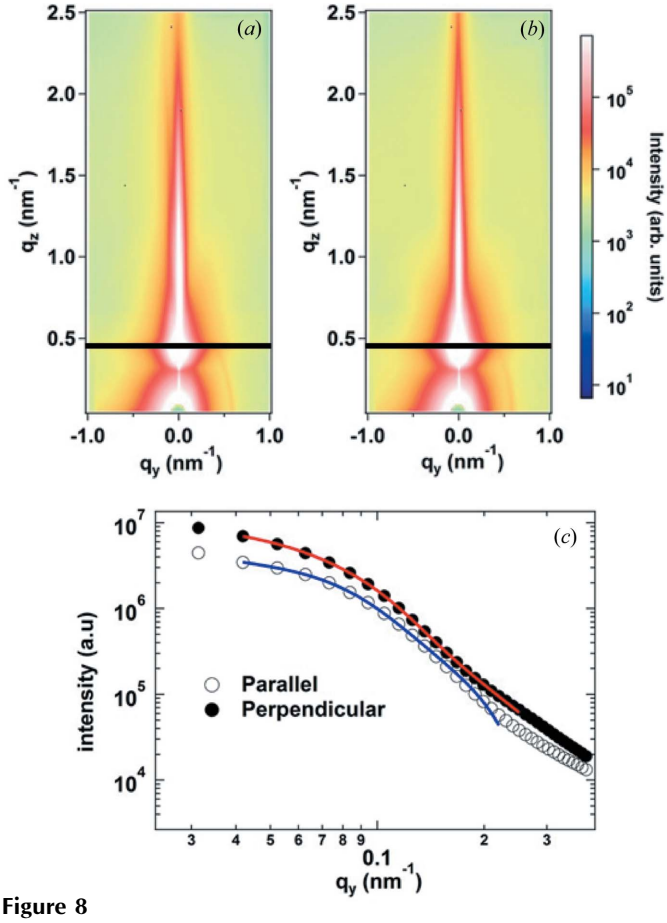

Figure 8
(*a*, *b*) GISAXS images of $EuSi_2$ nano-islands recorded at room temperature with the wavevector being, respectively, parallel and perpendicular to the vicinal steps. The black lines indicate the out-of-plane cuts made at the critical angle. (*c*) One-dimensional cuts (circles) at the critical angle (q_z = 0.45 nm^{-1}), parallel and perpendicular to the vicinal steps with the unified fitting (solid lines) to deduce the average lateral dimensions of the nano-islands.

cuts in the GISAXS patterns close to the critical angle ($q_z \simeq 0.45$ nm^{-1}) indicated by black lines [Figs. 8(*a*) and 8(*b*)].

The average lateral dimensions of the individual nano-islands are obtained by employing a less model-dependent unified fitting procedure, incorporating simultaneous Guinier and Porod fits, to the one-dimensional scattering intensity $I(q)$ (Beaucage, 1995; Sztucki *et al.*, 2007; Shyjumon *et al.*, 2008):

$$I(q) = G\exp\left(-q^2R_g^2/3\right) + B(q^*)^{-d_f}, \qquad (2)$$

where $G = \Delta\rho_e{}^2V^2$ is the Guinier pre-factor and B is a constant-scattering power-law specific pre-factor, d_f is the mass-fractal dimension and $q^* = q[\mathrm{erf}(qR_g/\sqrt{6})]^{-3}$ is the lower limit of the power-law decay regime. However, for the systematic study of more sophisticated systems with different geometries and correlations, one can use model-based simulations of full parameters using packages *IsGISAXS* (Lazzari, 2002; Lazzari *et al.*, 2007; Kaune *et al.*, 2009) and *FitGISAXS* (Babonneau, 2010). Fig. 8(*c*) shows the out-of-plane cuts, parallel and perpendicular to the steps and the corresponding unified fits to estimate the average lateral dimensions of the individual $EuSi_2$ nano-islands. The fit gives an average lateral

size of 75.6 ± 0.89 nm parallel and a somewhat smaller value of 68.6 ± 0.40 nm perpendicular to the vicinal steps. These values are slightly smaller compared with the dimensions derived from the AFM measurements on the same sample (Fig. 7*a*). This difference is caused by the fact that the sizes derived from the AFM images are affected by the convolution of the nano-object size with the AFM tip that has a finite size as well.

In order to investigate the thermal stability of the nano-islands the sample was heated to 1270 K for approximately 30 min and GISAXS images were recorded again at room temperature after the annealing. Figs. 9(*a*) and 9(*b*) show a comparison of the GISAXS images taken parallel to the steps before and after the high-temperature annealing. The main features of the GISAXS pattern are significantly changed. Fig. 9(*c*) plots the out-of-plane cuts and the unified fitting for the lateral sizes of the islands after annealing, revealing that the islands have reduced in size to 34.5 ± 0.96 nm parallel and 35.9 ± 0.90 nm perpendicular to the steps, which is almost by a factor of two smaller as compared with the corresponding values before heating. The AFM image recorded on the same sample after the heating experiment (Fig. 7*b*) confirms that the surface morphology has drastically changed. Namely, the average island size is reduced to ∼50 ± 5 nm in both directions, which is in agreement with the results from the GISAXS data. This result suggests that no further islands growth has taken place upon the post growth annealing. These observations differ from the reported $DySi_{2-x}$ islands coarsening *via* Ostwald ripening upon annealing at temperatures up to 1350 K (Zeman *et al.*, 2014).

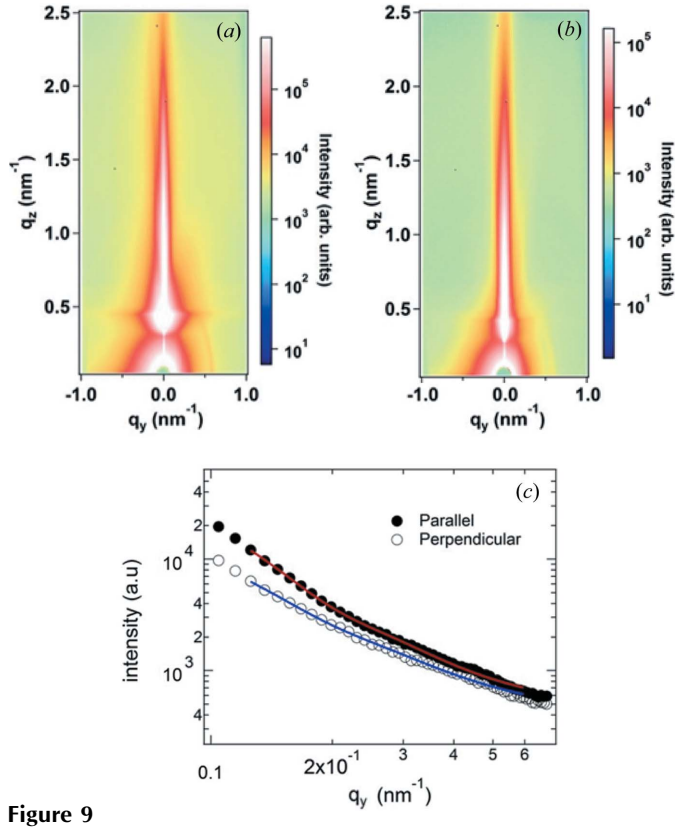

Figure 9
GISAXS images of the $EuSi_2$ nano-islands recorded parallel to the vicinal steps at room temperature, (*a*) before and (*b*) after annealing at 1270 K. (*c*) Illustration of how the horizontal (out-of-plane) cuts parallel and perpendicular to the steps (circles) and the corresponding fits (solid lines) for the sample after annealing.

Previous isothermal thermal-desorption spectroscopy (ITDS) experiments performed on europium silicide upon annealing up to 1000 K suggested that at such elevated temperature the silicides decompose and the Eu atoms desorb from the surface, while the Si atoms remain on the substrate (Krachino *et al.*, 2004). This phenomenon is observed in our annealing experiment as well, confirming that the processes taking place are silicide decomposition followed by desorption of Eu atoms from the Si(001) surface. Most likely the pronounced difference in the melting temperatures of Eu (1099 K) and Dy (1680 K) is the reason for the distinct behavior of europium and dysprosium silicides upon high-temperature post-growth annealing.

4. Conclusions and outlook

A portable UHV analysis chamber for X-ray scattering and spectroscopy studies of thin films and nanostructures at synchrotron radiation beamlines was constructed and brought into operation at the UHV-Analysis laboratory of ANKA, KIT. The available three configurations of this instrument offer the opportunity for *in situ* variable-temperature high-resolution XANES, RXES/RIXS, EXAFS, grazing-incidence diffraction and GISAXS studies on thin/ultrathin films and nanostructures deposited on a substrate. Some of the functionalities of the new instrument are demonstrated by investigation of the structure, stoichiometry and morphology changes upon high-temperature post-growth annealing of europium silicide film and nano-islands. The performed EXAFS and XANES study confirms the formation of $EuSi_2$ with tetragonal ($I4_1/amdS$) structure. The *in situ* GISAXS experiments reveal that upon annealing at 1270 K for 30 min a decomposition of the $EuSi_2$ nano-islands takes place and the Eu atoms desorb from the surface leading to an island size reduction by a factor of two. Islands coarsening *via* Ostwald ripening reported for $DySi_{2-x}$ nano-islands at high temperatures was not observed in $EuSi_2$ most likely due to the notably lower melting temperature of Eu compared with that of Dy.

The new instrument offers the opportunity for systematic *in situ* (under UHV conditions) studies of the thermal stability, morphology and structural changes upon annealing up to very high temperatures of various nanostructures deposited on a substrate. The low base pressure is a key element for surface-sensitive studies. Information about the atomic dynamics at the nanoscale can be extracted from temperature-dependent EXAFS studies of materials with coverages below one monolayer. Furthermore, the available free ports allow for controllable admission of various gases. Therefore, *in situ* investigation of oxidation phenomena would be possible using configurations A and B of the instrument. The rather compact UHV analysis chamber can transfer up to five samples grown and pre-characterized in the home laboratory to the beamlines of various synchrotron radiation sources. That offers new

possibilities for comprehensive *in situ* investigation of the interplay between structure, dynamics and magnetism of nanoscale materials supported on substrates by advanced X-ray scattering and spectroscopy methods.

This work is financially supported by the Initiative and Networking funds of the President of the Helmholtz Association and the Karlsruhe Institute of Technology *via* the Helmholtz University Young Investigators Groups 'Interplay between structure and lattice dynamics in epitaxial rare-earth nanostructures' contract VH-NG-625, 'Advanced synchrotron-based systematic investigations of actinide (An) and lanthanide (Ln) systems to understand and predict their reactivity' contract VH-NG-734, and the project 'Advanced investigations of model Ln nanostructures'. We are grateful to B. Krause, A. Weißhardt and H.-H. Gräfe for the support in the UHV-Analysis laboratory. Financial support for the UHV-Analysis laboratory *via* the Excellence Initiative within the project KIT-Nanolab@ANKA is acknowledged.

References

Babonneau, D. (2010). *J. Appl. Cryst.* **43**, 929–936.
Balandin, A. A. (2011). *Nat. Mater.* **10**, 569–581.
Beaucage, G. (1995). *J. Appl. Cryst.* **28**, 717–728.
Couet, S., Diederich, T., Schlage, K. & Röhlsberger, R. (2008). *Rev. Sci. Instrum.* **79**, 093908.
Döhrmann, R., Botta, S., Buffet, A., Santoro, G., Schlage, K., Schwartzkopf, M., Bommel, S., Risch, J. F., Mannweiler, R., Brunner, S., Metwalli, E., Müller-Buschbaum, P. & Roth, S. V. (2013). *Rev. Sci. Instrum.* **84**, 043901.
Evers, J., Oehlinger, G. & Weiss, A. (1977). *J. Solid State Chem.* **20**, 173–181.
Fanciulli, M. & Scarel, G. (2007). *Rare Earth Oxide Thin Films*, in *Topics in Applied Physics, Springer Series Vol. 106.* Berlin: Springer.
Glatzel, P., Sikora, M., Smolentsev, G. & Fernández-García, M. (2009). *Catal. Today*, **145**, 294–299.
Groot, F. M. F. de & Kotani, A. (2008). *Core Level Spectroscopy of Solids.* New York: Taylor and Francis.
Kaune, G., Ruderer, M. A., Metwalli, E., Wang, W., Couet, S., Schlage, K., Röhlsberger, R., Roth, S. V. & Müller-Buschbaum, P. (2009). *ACS Appl. Mater. Interfaces*, **1**, 353–360.
Krachino, T. V., Kuzmin, M. V., Loginov, M. V. & Mittsev, M. A. (2004). *Phys. Solid State*, **46**, 563–568.
Krause, B., Darma, S., Kaufholz, M., Gräfe, H.-H., Ulrich, S., Mantilla, M., Weigel, R., Rembold, S. & Baumbach, T. (2012). *J. Synchrotron Rad.* **19**, 216–222.
Lazzari, R. (2002). *J. Appl. Cryst.* **35**, 406–421.
Lazzari, R., Leroy, F. & Renaud, G. (2007). *Phys. Rev. B*, **76**, 125411.
Levine, J. R., Cohen, J. B., Chung, Y. W. & Georgopoulos, P. (1989). *J. Appl. Cryst.* **22**, 528–532.
Metwalli, E., Körstgens, V., Schlage, K., Meier, R., Kaune, G., Buffet, A., Couet, S., Roth, S. V., Röhlsberger, R. & Müller-Buschbaum, P. (2013). *Langmuir*, **29**, 6331–6340.
Ravel, B. & Newville, M. (2005). *J. Synchrotron Rad.* **12**, 537–541.
Rehr, J. J. & Albers, R. C. (2000). *Rev. Mod. Phys.* **72**, 621–654.
Renaud, G. (1998). *Surf. Sci. Rep.* **32**, 1–90.
Renaud, G., Ducruet, M., Ulrich, O. & Lazzari, R. (2004). *Nucl. Instrum. Methods Phys. Res. B*, **222**, 667–680.
Renaud, G., Lazzari, R., Revenant, C., Barbier, A., Noblet, M., Ulrich, O., Leroy, F., Jupille, J., Borensztein, Y., Henry, C. R., Deville, J. P., Scheurer, F., Mane-Mane, J. & Fruchart, O. (2003). *Science*, **300**, 1416–1419.
Rothe, J., Butorin, S., Dardenne, K., Denecke, M. A., Kienzler, B., Löble, M., Metz, V., Seibert, A., Steppert, M., Vitova, T., Walther, C. & Geckeis, H. (2012). *Rev. Sci. Instrum.* **83**, 43105.
Santoro, G., Yu, S., Schwartzkopf, M., Zhang, P., Vayalil, S. K., Risch, J. F. H., Rübhausen, M. A., Hernández, M., Domingo, C. & Roth, S. V. (2014). *Appl. Phys. Lett.* **104**, 243107.
Schwartzkopf, M., Buffet, A., Körstgens, V., Metwalli, E., Schlage, K., Benecke, G., Perlich, J., Rawolle, M., Rothkirch, A., Heidmann, B., Herzog, G., Müller-Buschbaum, P., Röhlsberger, R., Gehrke, R., Stribeck, N. & Roth, S. V. (2013). *Nanoscale*, **5**, 5053–5062.
Seiler, A., Ibrahimkutty, S., Bauder, O., Prüßmann, T., Vitova, T., Pradip, R., Baumbach, T., Fiederle, M. & Stankov, S. (2014). *J. Cryst. Growth.* **407**, 74–77.
Shyjumon, I., Rappolt, M., Sartori, B., Amenitsch, H. & Laggner, P. (2008). *Rev. Sci. Instrum.* **79**, 043905.
Slobodskyy, T., Schroth, P., Grigoriev, D., Minkevich, A. A., Hu, D. Z., Schaadt, D. M. & Baumbach, T. (2012). *Rev. Sci. Instrum.* **83**, 105112.
Snider, G. S. & Williams, R. S. (2007). *Nanotechnology*, **18**, 035204.
Stankov, S., Rüffer, R., Sladecek, M., Rennhofer, M., Sepiol, B., Vogl, G., Spiridis, N., Slezak, T. & Korecki, J. (2008). *Rev. Sci. Instrum.* **79**, 045108.
Stierle, A., Steinhäuser, A., Rühm, A., Renner, F. U., Weigel, R., Kasper, N. & Dosch, H. (2004). *Rev. Sci. Instrum.* **75**, 5302.
Sztucki, M., Narayanan, T. & Beaucage, G. (2007). *J. Appl. Phys.* **101**, 114304.
Vitova, T., Hormes, J., Peithmann, K. & Woike, T. (2008). *Phys. Rev. B*, **77**, 144103.
Vitova, T., Kvashnina, O., Nocton, G., Sukharina, G., Denecke, M. A., Butorin, S. M., Mazzanti, M., Caciuffo, R., Soldatov, A., Behrends, T. & Geckeis, H. (2010). *Phys. Rev. B*, **82**, 235118.
Yu, S., Santoro, G., Sarkar, K., Dicke, B., Wessels, P., Bommel, S., Döhrmann, R., Perlich, J., Kuhlmann, M., Metwalli, E., Risch, J. F. H., Schwartzkopf, M., Drescher, M., Müller-Buschbaum, P. & Roth, S. V. (2013). *J. Phys. Chem. Lett.* **4**, 3170–3175.
Zeman, M. C., Nemanich, R. J. & Sunda-Meya, A. (2014). *J. Mater. Sci.* **49**, 1812–1823.